

A multi-technique detection of an eccentric giant planet around accelerating star HD 57625

D. Barbato¹, D. Mesa¹, V. D’Orazi^{2,1}, S. Desidera¹, A. Ruggieri³, J. Farinato¹, L. Marafatto¹, E. Carolo¹, D. Vassallo¹, S. Ertel^{4,5}, J. Hom⁴, R.M. Anche⁴, F. Battaini¹, A. Becker⁵, M. Bergomi¹, F. Biondi^{6,1}, A. Cardwell⁵, P. Cerpelloni¹, G. Chauvin⁷, S. Chinellato¹, C. Desgrange^{7,8}, S. Di Filippo¹, M. Dima¹, T.S. Gomes Machado^{1,9}, R. Gratton¹, D. Greggio¹, Th. Henning⁷, M. Kenworthy¹⁰, F. Laudisio¹, C. Lazzoni¹, J. Leisenring⁴, L. Lessio¹, A. Lorenzetto¹, L. Mohr⁷, M. Montoya⁴, G. Rodeghiero¹¹, J. Patience¹², J. Power⁵, D. Ricci¹, K.K.R. Santhakumari¹, A. Sozzetti¹³, G. Umbriaco^{14,1}, M. Vega Pallauta², V. Viotto¹, and K. Wagner⁴

¹ INAF – Osservatorio Astronomico di Padova, Vicolo dell’Osservatorio 5, I-35122, Padova, Italy
e-mail: domenico.barbato@inaf.it

² Department of Physics, University of Rome Tor Vergata, via della Ricerca Scientifica 1, 00133, Rome, Italy

³ INAF – Osservatorio Astrofisico di Catania, Via S. Sofia 78, 95123 Catania, Italy

⁴ Department of Astronomy and Steward Observatory, The University of Arizona, 933 North Cherry Ave, Tucson, AZ85721, USA

⁵ Large Binocular Telescope Observatory, The University of Arizona, 933 North Cherry Ave, Tucson, AZ85721, USA

⁶ Max Planck Institute for extraterrestrial Physics, Gießenbachstraße 1, 85748 Garching bei München, Germany

⁷ Max Planck Institute for Astronomy, Königstuhl 17, 69117 Heidelberg, Germany

⁸ Univ. Grenoble Alpes, CNRS, IPAG, F-38000 Grenoble, France

⁹ Department of Physics and Astronomy, University of Padova, Vicolo dell’Osservatorio 3, 35122 Padova, Italy

¹⁰ Leiden Observatory, University of Leiden, PO Box 9513, 2300 RA Leiden, The Netherlands

¹¹ INAF Osservatorio Astronomico d’Abruzzo, Via Mentore Maggini, I-64100 Teramo, Italy

¹² School of Earth and Space Exploration, Arizona State University, Tempe, AZ 85281, USA

¹³ INAF – Osservatorio Astrofisico di Torino, Via Osservatorio 20, 10025, Pino Torinese, Italy

¹⁴ Dipartimento di Fisica e Astronomia “Augusto Righi” - Alma Mater Studiorum Università di Bologna, via Piero Gobetti 93/2 - 40129, Bologna, Italy

Received <date> / Accepted <date>

ABSTRACT

Context. The synergy between different detection methods is a key asset in exoplanetology, allowing for both precise characterization of detected exoplanets and robust constraints even in the case of non-detection. Recently, the interplay between imaging, radial velocities and astrometry has produced significant advancements in exoplanetary science.

Aims. We report a first result of an ongoing survey performed with SHARK-NIR, the new high-contrast near-infrared imaging camera at the Large Binocular Telescope, in parallel with LBTI/LMIRCam in order to detect planetary companions around stars with significant proper motion anomaly. In this work we focus on HD 57625, a F8 star for which we determine a $4.8_{-2.9}^{+3.7}$ Ga age, exhibiting significant astrometric acceleration and for which archival radial velocities hint at the presence of a previously undetected massive long-period companion.

Methods. We analyse the imaging data we collected with SHARK-NIR and LMIRCam in synergy with the available public SOPHIE radial velocity time series and Hipparcos-Gaia proper motion anomaly. With this joint multi-technique analysis, we aim at characterizing the companion responsible for the astrometric and radial velocity signals.

Results. The imaging observations result in a non-detection, indicating the companion to be in the substellar regime. This is confirmed by the synergic analysis of archival radial velocity and astrometric measurements resulting in the detection of HD 57625 b, a $8.43_{-0.91}^{+1.1}$ M_{Jup} planetary companion with an orbital separation of $5.70_{-0.13}^{+0.14}$ au and $0.52_{-0.03}^{+0.04}$ eccentricity.

Conclusions. HD 57625 b joins the small but growing population of giant planets in outer orbits with true mass determination provided by the synergic usage of multiple detection methods, proving once again the importance of multi-technique analysis in providing robust characterization of planetary companions.

Key words. techniques: image processing – techniques: radial velocities – astrometry – planetary systems – planets and satellites: detection – stars: individual: HD 57625

1. Introduction

As the continuous growth of exoplanetology results in both new detections of planetary companions and refined and more in-depth characterization of known systems, the development of new and more precise instrumentation keeps fueling the exploration of all facets of exoplanetary science. As a result, the syn-

ergic interplay between the many discovery techniques available in the field becomes an increasingly key asset in furthering our search for exoplanetary systems. Among these various techniques, direct imaging is especially suited to detect giant companions on wide orbits ($\gtrsim 10$ au) around young stars, and as such is able to provide an unparalleled view on the early stages of exoplanet formation and evolution processes. Some notable

examples of exoplanetary systems discovered and characterized by imaging observations include HR 8799 (Marois et al. 2008, 2010), GJ 504 (Kuzuhara et al. 2013), 51 Eri (Macintosh et al. 2015), PDS 70 (Keppler et al. 2018; Müller et al. 2018; Haffert et al. 2019) and AF Lep (Mesa et al. 2023; Franson et al. 2023; De Rosa et al. 2023).

Although successful, as every other discovery technique, the imaging method is characterized by drawbacks limiting its potential. Chiefly, imaging observations are highly time-consuming, requiring long exposures that can easily reach a few hours depending on target star characteristics, therefore impacting the scientific yield of observing nights. Additionally, the return of imaging surveys is intrinsically limited by the observed low occurrence rate of the wide-orbit massive companions for which the technique is ideally suited, often resulting in the need to observe hundreds of targets to successfully detect a low number of companions in the planetary mass regime (see e.g. Galicher et al. 2016; Nielsen et al. 2019; Vigan et al. 2021). Indeed, demographic studies suggest that the majority of giant planets have orbits with semi-major axes between 1 and 10 au, peaking for example at ~ 3 au for M-dwarf host stars (see e.g. Meyer et al. 2018), putting a significant portion of giant exoplanets beyond the technical capabilities of current high-contrast imagers. As such, the relatively low imaging detection rate of planetary-mass companions represents a significant obstacle in bringing to full fruition the potential of imaging surveys.

It is therefore clear that the usage of pre-selection criteria to identify the stellar targets more likely to host planetary companions within the reach of current imaging instruments is essential to enhance the scientific yield of imaging surveys. Such criteria, providing preliminary hints of the presence of planetary-mass companions and allowing for targeted observations, arise from the synergic usage of other detection techniques, again highlighting the increasing importance that the interplay between different techniques currently has in exoplanetology.

A typical example of such pre-selection criteria is represented by the identification in radial velocity (RV) time series of either a full Keplerian orbital variation or trends hinting at the presence of undetected massive companions having an orbital period longer than the time span of the available RV observations, possibly ideal for imaging follow-up observations and robust detection. Successful examples of this strategy in the recent literature include the direct detection of brown dwarf (BD) GJ 758 B (Calissendorff & Janson 2018) and exoplanets β Pic c (Nowak et al. 2020), HD 206893 c (Hinkley et al. 2023) and ϵ Ind Ab (Matthews et al. 2024) with imaging observations confirming previous RV-only results.

Another successful pre-selection criterion focuses on the exploitation of the high-precision absolute astrometric catalogs produced by the Hipparcos (van Leeuwen 2007) and Gaia (Gaia Collaboration et al. 2016) missions, in the latter case utilizing its second and third major data releases (DR2 and DR3, see Gaia Collaboration et al. 2018, 2023). Specifically, a statistically significant difference between the long-term proper motion vector of a star common to the two catalogs and the short-term Gaia (and Hipparcos) measurements, typically referred to as proper motion anomaly (PMA) will indicate the presence of a perturbing companion. The recent release of Hipparcos-Gaia astrometric acceleration catalogs (Brandt 2021; Kervella et al. 2022) has fueled the usage of significant PMA as pre-selection tool for imaging surveys and resulted in the detection of brown dwarfs (BDs) companions (see e.g. Calissendorff & Janson 2018; Currie et al. 2020; Bonavita et al. 2022) and is recently starting to show its ex-

oplanetary potential in the detection of AF Lep b (see e.g. Mesa et al. 2023; De Rosa et al. 2023; Franson et al. 2023).

In both cases, imaging observations can either successfully detect the planetary companion responsible for the RV trend or the significant PMA or, in the case of a non-detection, provide robust constraints on both companion mass and orbital separation based on the detection capabilities of the specific instrument (see e.g. Mesa et al. 2022). As such, even a non-detection can advance the characterization of candidate planetary companions and fuel follow-up observations, once more proving the opportunities represented by the synergic usage of multi-technique analysis.

As such, the observation of a sample of stars exhibiting significant astrometric acceleration is a key scientific program selected for the early science validation phase of SHARK-NIR (Farinato et al. 2022, 2023; Marafatto et al. 2022), a high-contrast camera operating in the Y, J and H near-infrared bands that has recently been installed on the left arm of the Large Binocular Telescope (LBT) in Arizona. The instrument is designed to fully take advantage of the extreme adaptive optics (AO) correction performed by the LBT AO system SOUL (Single Conjugated Adaptive Optics Upgrade for LBT, see Pinna et al. 2016; Pinna et al. 2023). Indeed, detailed simulations have shown that SHARK-NIR is able to achieve in good weather Strehl ratios up to more than 90% and contrast levels down to 10^{-6} at separations of 300-500 mas (Carolo et al. 2018). The instrument's location at the LBT common center-bent Gregorian focus allows for synergic simultaneous high-contrast observations with SHARK-VIS (operating in visible light, see Pedichini et al. 2022) and LBTI/LMIRCam (operating in J to M infrared bands, see Skrutskie et al. 2010; Leisenring et al. 2012). Installed on LBT in October 2022, SHARK-NIR has afterwards completed its commissioning phase and is now undertaking its early science validation runs (as detailed in Barbato et al. 2024) directly addressing its scientific goals, namely the detection and characterization of giant extrasolar planets, disks and jets around young stars, active galactic nuclei and Solar System small bodies.

In this work we present the first results from the accelerating stars survey to be further presented in Mesa et al. (2024), performed with SHARK-NIR during its first early science runs, more specifically focusing on the observations undertaken in February 2024 on star HD 57625 (HIP 36014). This star was selected as part of SHARK-NIR early science observations both by virtue of its significant PMA reported in Kervella et al. (2022), with a signal-to-noise ratio (SNR) of 11.04, and archival SOPHIE RV time series showing a clear long-term variation, both characteristics hinting at the presence of a previously undetected long-period giant planetary companion that we present and characterize for the first time via a multi-technique analysis.

This paper is organized as follows: in Sect. 2 we provide an updated description of the target star physical characteristic, before moving on to describe the SHARK-NIR and LMIRCam observations and data analysis in Sect. 3, the analysis of the archival radial velocity data in Sect. 4 and of the proper motion anomaly measurements in Sect. 5. Finally, we perform a multi-technique detection completeness characterization of the target star in Sect. 6, before concluding and discussing our results and future perspectives in Sect. 7.

2. HD 57625 stellar characteristics

HD 57625 (HIP 36014) is a F8 star distant 44.24 pc from the Sun and estimated to be 6.29 Ga old (Gaia Collaboration et al. 2023)

Table 1. Stellar parameters for HD 57625.

| HD 57625 | |
|--------------------------------------------------------|---------------------------------------------------|
| HIP | 36014 |
| Gaia DR3 | 989016898234332416 |
| α (J2000) ^a | 7 ^h 25 ^m 18.03 ^s |
| δ (J2000) ^a | +56°34′8.96″ |
| ϖ (mas) ^a | 22.5622 ± 0.0263 |
| μ_α (mas a ⁻¹) ^a | -55.181 ± 0.020 |
| μ_δ (mas a ⁻¹) ^a | -59.102 ± 0.016 |
| $\Delta\mu_\alpha$ (mas a ⁻¹) ^b | 0.340 ± 0.026 |
| $\Delta\mu_\delta$ (mas a ⁻¹) ^b | -0.141 ± 0.021 |
| dV_t (m s ⁻¹) ^b | 77.34 ± 7.01 |
| RV_{sys} (km s ⁻¹) ^c | 4.673 ± 0.0024 |
| B_T (mag) ^d | 8.41 ± 0.01 |
| V_T (mag) ^d | 7.75 ± 0.01 |
| B (mag) ^e | 8.41 ± 0.01 |
| V (mag) ^e | 7.75 ± 0.01 |
| J (mag) ^e | 6.581 ± 0.019 |
| H (mag) ^e | 6.364 ± 0.038 |
| K (mag) ^e | 6.276 ± 0.017 |
| WISE1 (mag) ^g | 6.214 ± 0.067 |
| WISE2 (mag) ^g | 6.214 ± 0.023 |
| WISE3 (mag) ^g | 6.293 ± 0.015 |
| WISE4 (mag) ^g | 6.303 ± 0.055 |
| G (mag) ^c | 7.555 ± 0.003 |
| G_{BP} (mag) ^c | 7.842 ± 0.003 |
| G_{RP} (mag) ^c | 7.098 ± 0.004 |
| Spectral Type ^h | F8 |
| M_\star (M _⊙) ⁱ | 1.040 ^{+0.078} _{-0.080} |
| R_\star (R _⊙) ⁱ | 1.126 ^{+0.046} _{-0.040} |
| ρ_\star (g cm ⁻³) ⁱ | 1.02 ^{+0.15} _{-0.14} |
| L_\star (L _⊙) ⁱ | 1.466 ^{+0.13} _{-0.093} |
| Age (Ga) ⁱ | 4.8 ^{+3.7} _{-2.9} |
| T_{eff} (K) ^j | 5961.78 ± 43.33 |
| $\log g$ (cgs) ^j | 4.47 ± 0.08 |
| [Fe/H] ^j | -0.04 ± 0.02 |
| $v \sin i$ (km s ⁻¹) ^k | 1.8 |
| S_{MW}^l | 0.1898 ± 0.0367 |
| H α ^l | 0.1294 ± 0.0060 |
| Na I ^l | 0.4962 ± 0.0157 |
| $P_{\text{rot, Noyes}}$ (d) ^l | 22.25 ± 4.23 |
| $P_{\text{rot, Mamajek}}$ (d) ^l | 22.47 ± 4.96 |

Notes. ^(a) retrieved from Gaia Data Release 3 (Gaia Collaboration et al. 2023) ^(b) retrieved from Kervella et al. (2022) ^(c) retrieved from Gaia Data Release 2 (Soubiran et al. 2018) ^(d) retrieved from Høg et al. (2000) ^(e) retrieved from Zacharias et al. (2012) ^(f) retrieved from Cutri et al. (2003) ^(g) retrieved from Cutri et al. (2021) ^(h) retrieved from Cannon & Pickering (1993) ⁽ⁱ⁾ obtained from the SED fitting discussed in Sect. 2 ^(j) obtained from the spectroscopic analysis discussed in Sect. 2 ^(k) retrieved from Głęboccki & Gnačić (2005) ^(l) obtained from the SOPHIE spectra analysis discussed in Sect. 2

with a reported mass of $1.16 \pm 0.06 M_\odot$ (Kervella et al. 2022). As mentioned in Sect. 1, the astrometric acceleration catalog presented in (Kervella et al. 2022) reports a strong PMA signal having a SNR of 11.04, hinting at the likely presence of an unseen massive companion.

HD 57625 is part of a wide binary system, with a fainter stellar companion (2MASS J07251770+5634002, Gaia DR3 989016790859521280, $G = 15.17$ mag) located at 10″ corresponding to a projected separation of ~ 440 au. The physical association is supported by the Gaia astrometric parameters.¹ A mass of $\sim 0.2 M_\odot$ is estimated for the companion from the main sequence relationships by Pecaut & Mamajek (2013)². We note that the observed PMA is not compatible with this distant low-mass stellar companion, as we will discuss in Sect. 5.

For further characterization, we exploited archival spectra taken with SOPHIE as described in Sect. 4 to derive atmospheric parameters and metallicity. We employed LOTUS (non-LTE Optimization Tool Utilized for the derivation of atmospheric Stellar parameters) by Li & Ezzeddine (2023)³ adopting an optimised linelist for solar analogues, which is available upon request. This tool calculates parameters using the equivalent width (EW) method for Fe I and II lines, incorporating a generalized curve of growth approach to account for EW dependencies on the corresponding atmospheric stellar parameters. A global differential evolution optimization algorithm is applied to extract the fundamental parameters. Furthermore, LOTUS provides precise uncertainties for each stellar parameter through a Markov Chain Monte Carlo algorithm. The resulting spectroscopic effective temperature (T_{eff}) is 5962 ± 43 K, the stellar gravity is $\log g = 4.47 \pm 0.08$ dex, the microturbulent velocity is $V_{\text{mic}} = 1.00 \pm 0.03$ km s⁻¹, and the iron abundance [Fe/H] is -0.04 ± 0.02 (random errors). These results are consistent, within observational uncertainties, with the available estimates in the literature.

In order to have an updated and homogeneous characterization of the physical properties of HD 57625 for our analysis, we fit its stellar spectral energy distribution (SED) using the MESA Isochrones and Stellar Tracks (MIST) (Dotter 2016; Choi et al. 2016) via the IDL suite EXOFASTv2 (Eastman et al. 2019). With this method, the stellar parameters are simultaneously constrained by the SED and the MIST isochrones, since the SED primarily constrains the stellar radius R_\star and effective temperature T_{eff} , while a penalty for straying from the MIST evolutionary tracks ensures that the resulting star is physical in nature (see Eastman et al. 2019, for more details on the method). We considered all available archival magnitudes from Tycho B_T and V_T bands (Høg et al. 2000), Johnson’s B , V and 2MASS J , H , and K bands from the UCAC4 catalog (Zacharias et al. 2012; Cutri et al. 2003), WISE bands (Cutri et al. 2021), and Gaia G , G_{BP} , and G_{RP} bands (Gaia Collaboration et al. 2023), imposing Gaussian priors on the star’s effective temperature T_{eff} , and metallicity [Fe/H] based on their respective values we obtain from the activity indexes analysis detailed in the previous paragraph, as well as on the stellar parallax ϖ based on Gaia DR3 astrometric measurement (Gaia Collaboration et al. 2023). We list in Table 1 the

¹ We additionally note that HD 57625 is included in the current version of the Washington Double Star (WDS) catalog as a triple system, but both the listed components, namely HD 57667 (WDS J07254+5633A) and 2MASS J07251750+5633363 (WDS J07254+5633C) are clearly ruled out as physical companions by the largely discrepant astrometric parameters in Gaia DR3.

² Updated version (2022.04.16) at https://www.pas.rochester.edu/~emamajek/EEM_dwarf_UBVIJHK_colors_Teff.txt

³ <https://lotus-nlte.readthedocs.io/en/latest/>

Table 2. SOPHIE and SOPHIE+ measurements for HD 57625

| BJD | RV (km s ⁻¹) | FWHM (km s ⁻¹) | BIS (km s ⁻¹) | S_{MW} | H α | Na I |
|------------|-----------------------------|-------------------------------|------------------------------|---------------------|---------------------|---------------------|
| 2454051.70 | 4.7913 \pm 0.0027 | 7.7459 | 0.0000 | 0.3768 \pm 0.0021 | 0.1490 \pm 0.0012 | 0.5103 \pm 0.0023 |
| 2454053.66 | 4.7942 \pm 0.0027 | 7.7566 | 0.0000 | 0.3277 \pm 0.0016 | 0.1416 \pm 0.0009 | 0.4844 \pm 0.0016 |
| 2454872.47 | 4.6845 \pm 0.0027 | 7.7541 | 0.0038 | 0.1900 \pm 0.0028 | 0.1373 \pm 0.0014 | 0.4900 \pm 0.0028 |
| 2454893.44 | 4.6813 \pm 0.0026 | 7.7820 | -0.0048 | 0.2099 \pm 0.0027 | 0.1441 \pm 0.0014 | 0.5015 \pm 0.0028 |
| 2454894.36 | 4.6813 \pm 0.0026 | 7.7816 | 0.0078 | 0.2524 \pm 0.0031 | 0.1386 \pm 0.0014 | 0.5044 \pm 0.0027 |
| ... | ... | ... | ... | ... | ... | ... |

Notes. Data are available at the CDS and on the SOPHIE archive. A portion is shown here for guidance regarding its form and content.

resulting best-fit stellar parameters, as well as the other parameters resulting from all analysis detailed in this Section.

The resulting age from isochrones is in general agreement with the evidences from other indicators, such as the low activity inferred from the SOPHIE spectra discussed in the next paragraph, X-ray non detection in Rosat All Sky Survey (Voges et al. 1999, 2000), slow rotation (Głęboczi & Gnaniński 2005), thin disk kinematics (Gaia Collaboration et al. 2021). Therefore, we adopt the isochrone age and corresponding stellar mass in the rest of this work.

To determine the activity level of HD 57625 and check whether the detected RV signal (see Sect. 4) is related to an activity cycle, we use the Python tool ACTIN2⁴ (Gomes da Silva et al. 2018, 2021) to extract activity indicators from the SOPHIE spectra. In particular, we used the following indicators: emission from the Ca II H & K lines (S_{MW}), H α , and Na I D2 line, whose median values and corresponding 1 σ error bars are shown in Table 1. We plot in Fig 3 the resulting activity indexes time series, as well as the RV, full width at half maximum (FWHM) and bisector inverse span (BIS) we analyse in detail in Sect. 4. We produce generalized Lomb-Scargle (GLS) periodograms for each activity index time series, finding for S_{MW} a long-period oscillation (>5000 d), while for H α we found a very significant (FAP \ll 0.001%) peak at 11.35 d, as well as another long-period (>5000 d) trend. Interestingly, the 11.35 d peak is exactly half the rotation period of the star derived from the S_{MW} time series using the equations by Noyes et al. (1984) and Mamajek & Hillenbrand (2008). In particular, we obtained $P_{rot,Noyes} = 22.25 \pm 4.23$ d and $P_{rot,Mamajek} = 22.47 \pm 4.96$ d, in perfect agreement with each other. For the Na I, we find a low-significance (FAP = 2.6%) principal peak at 4 d, indicating no strong signal in this time series. From this analysis, we conclude that HD 57625 lacks any strong activity, excluding possible long-period cycles inferred from the S_{MW} and H α time series. We additionally note that all activity indexes analysed appear to be uncorrelated to the observed large RV variation, with the largest Pearson correlation coefficient ρ being that of S_{MW} hinting at a moderate correlation ($\rho = 0.49$) which we will further address in Sect. 4.

3. Imaging observations and analysis

We observed HD 57625 with SHARK-NIR on the night of February 24th 2024 UT using the broadband H filter (central wavelength at 1.6 μ m and 0.218 μ m bandwidth) and the instrument's Gaussian coronagraph that has an inner Working Angle (IWA) of 120 mas, which at the 44.24 pc distance of HD 57625 corresponds to a 5.30 au separation. We obtained a total of 208

frames each with a 18.7257 s detector integration time (DIT) for a total exposure time of \sim 3895 s (\sim 65 minutes). The observations were performed in pupil stabilized mode in order to implement angular differential imaging (ADI, see e.g. Marois et al. 2006), allowing a total rotation of the field of view (FOV) of 40.58 deg. During the observations the seeing varied between 0.94'' and 2.19''. We also took an image with the stellar PSF unocculted by the coronagraph both before and after the main coronagraphic observations, to be able to correctly estimate the contrast on the scientific image. These frames were taken introducing in the optical path a neutral density filter (ND3) to avoid the detector saturation.

In addition to the SHARK-NIR observations we simultaneously observed our target with LBTI/LMIRCam (Skrutskie et al. 2010; Leisenring et al. 2012) on the right arm of LBT. These observations were performed in the L' spectral band (central wavelength at 3.7 μ m and 0.58 μ m bandwidth) using the vector-apodizing phase plate coronagraph (vAPP, Doelman et al. 2021), with an IWA of 246 mas corresponding for HD 57625 to a 10.88 au separation. In this case we obtained 3200 frames, each of them with a DIT of 1.51085 s for a total exposure time of 4834.72 s (80.58 minutes). The LMIRCam observations were also performed in pupil stabilized mode with a total rotation of the FOV of 43.38 deg.

Because of the non-destructive charge transfer capability of the SHARK-NIR scientific detector, each individual exposure is a ramp, i.e. a set of reads taken at uniform time intervals. The raw ramps were first reduced using a Python pipeline specifically developed for the SHARK-NIR detector, performing reference pixel correction, bias subtraction, and linearity correction. Finally, the software collapses the ramps into single frames using an up-the-ramp sampling algorithm.

The SHARK-NIR data were then post-processed using the pipeline custom designed for the instrument and written in Python. First, we subtracted the dark and divided by the flat-field images. For our analysis, we meticulously fine-centered each frame by utilizing the four symmetrical spots created by the SHARK-NIR internal deformable mirror. Additionally, we conducted a selection process to identify and exclude any low-quality frames such as those where the star was not adequately masked by the coronagraph. Finally, we applied a post-processing procedure based on the ADI method and exploiting the principal components analysis (PCA; Soummer et al. 2012; Amara & Quanz 2012) algorithm.

Similarly, each LMIRCam exposure is a ramp composed in this case of two frames taken at different intermediate exposure times, the first one with a time equal to just 13.7 ms and the last one corresponding to the total exposure time. As a first step, we subtracted the first image of the ramp data cube from the last one to remove the bias from the science data. The data were

⁴ <https://actin2.readthedocs.io/en/latest/index.html>

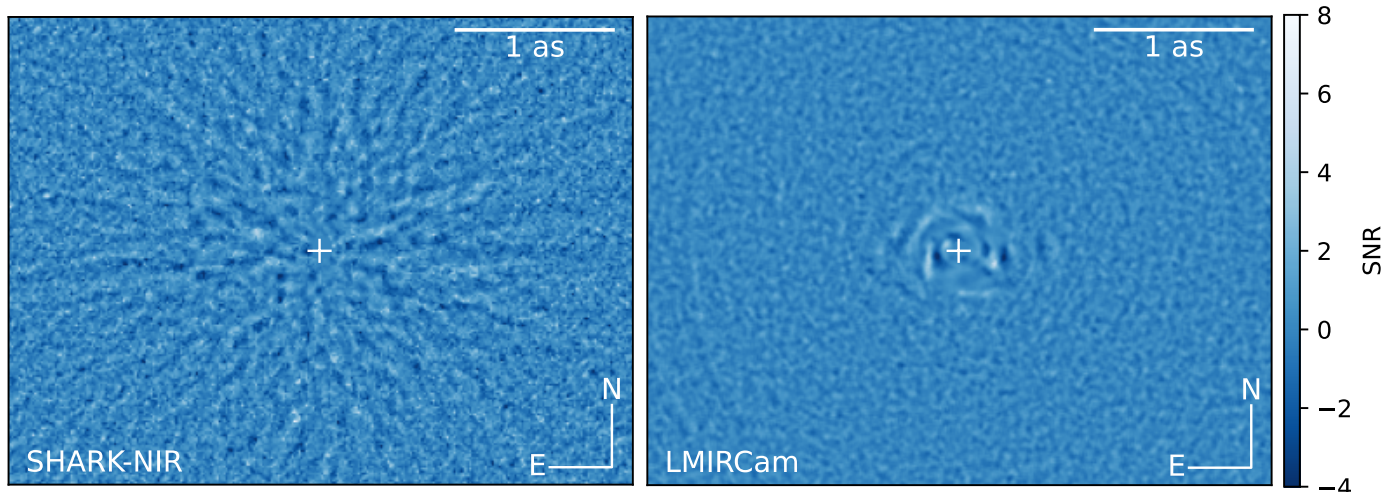


Fig. 1. Final SNR map of the inner region around HD 57625 obtained using the SHARK-NIR H-band (*left panel*) and the LMIRCam L'-band data (*right panel*), a white cross marking the position of the central star. In both cases the images were obtained using a PCA technique subtracting 10 principal components.

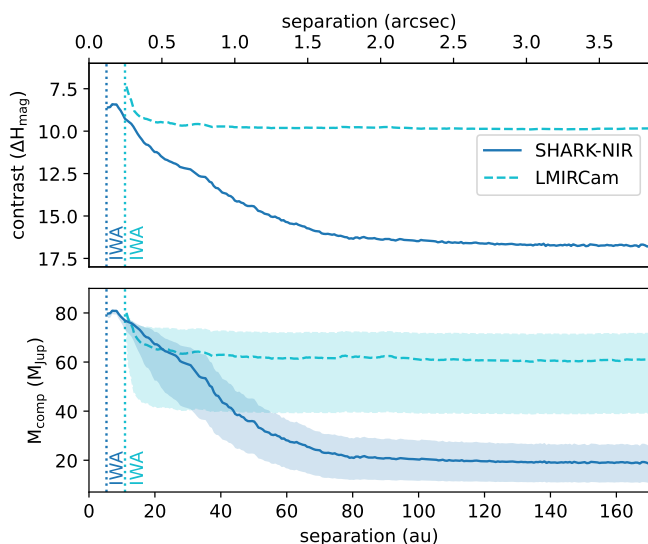


Fig. 2. *Top panel:* contrast curve for the imaging observation of HD 57625 conducted on the night of February 24th 2024 UT. *Bottom panel:* mass limits derived using the AMES-COND models, the thick curve corresponding to the nominal 4.8 Ga stellar age, the shaded region corresponding to the age uncertainty. In both panels, the blue solid curves refer to the SHARK-NIR H-band observations and the cyan dashed lines refer to the LMIRCam L'-band observation, with similarly colour-coded vertical dotted lines indicating the Inner Working Angle (IWA) of each instrument.

taken with two different nodding positions called A and B. We then subtracted from each image a median of the 100 closest images in time from the opposite nod position, in order to subtract thermal background flux from all frames obtained at MIR wavelengths without needing to obtain sky frames. Finally, we applied a PCA-based post-processing similar to what was done for the SHARK-NIR data.

The final images obtained for both instruments from the procedure described above are displayed in Fig. 1. No source with $\text{SNR} > 5$ is detected on either image, allowing us to conclude that no companion has been detected orbiting around HD 57625 dur-

ing our observations. However, as discussed in Sect. 1 even a non-detection in imaging data can be successfully used to provide robust limits on the unseen companion producing the PMA and RV signals.

In Fig. 2 we show the SHARK-NIR and LMIRCam observation contrast curve as a function of separation as well as the respective mass limits derived using the AMES-COND models (Allard et al. 2003) assuming the stellar age range of $4.8^{+3.7}_{-2.9}$ Ga derived in Sect. 2. From these mass limits, it is clear that while any planetary companion of HD 57625 would not have been detected, both SHARK-NIR and LMIRCam would have been able to detect any stellar companion at all separations above the aforementioned respective coronagraphic limits of 5.3 au and 10.88 au, as well as very wide and massive brown dwarfs. Therefore, the non-detection produced by our parallel SHARK-NIR and LMIRCam imaging observations in H and L' infrared bands allows to confirm the substellar and likely planetary nature of the companion producing the PMA and RV signal of HD 57625.

4. Radial velocity analysis

As mentioned in Sect. 1, the archival radial velocity time series available for HD 57625 are characterized by the presence of a clear long-term trend hinting at the presence of a wide-orbit massive companion. Specifically, in this Section we focus on the publicly available RV measurements collected by the spectrograph SOPHIE (Perruchot et al. 2008), mounted on the 1.93 m telescope at the Haute-Provence Observatory in France. We additionally note that in June 2011 the fibre link of the instrument was upgraded (Bouchy et al. 2013), introducing an offset between the data collected before and after this date. In the following we therefore treat the RV measurements taken for HD 57625 before and after the fibre upgrade as independent datasets named as SOPHIE and SOPHIE+, respectively.

We retrieve a total of 70 publicly available radial velocity measurements (11 before the fibre upgrade and 59 after) from the SOPHIE archive⁵ (Moultaka et al. 2004), spanning from November 12th 2006 to October 2nd 2019 and therefore providing an observational baseline of 4708 d with a median RV

⁵ <http://atlas.obs-hp.fr/sophie>

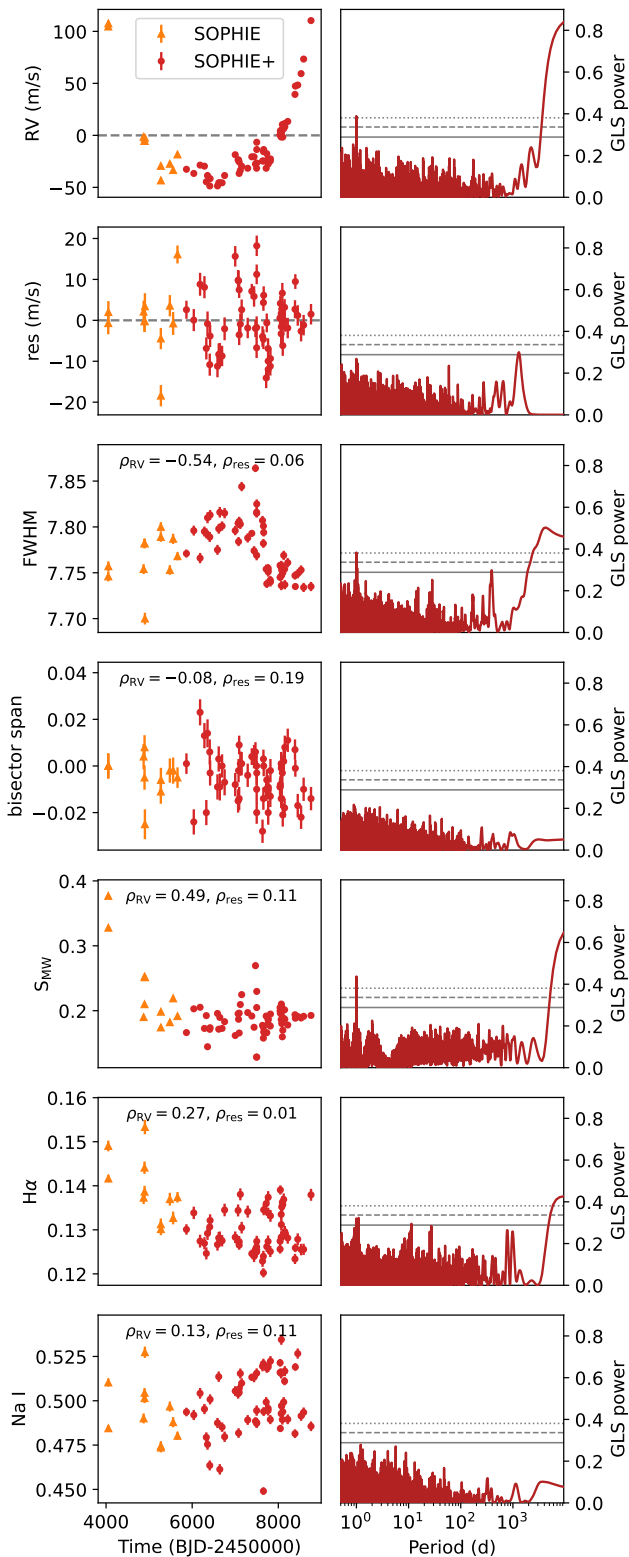


Fig. 3. *Left panels:* time series for the SOPHIE (orange triangles) and SOPHIE+ (red circles) radial velocity data of HD 57625, residual time series obtained after removing the detected Keplerian signal and activity indexes. For the activity indexes time series, the Pearson correlation coefficient with both original and residual RVs are noted. *Right panels:* corresponding generalised Lomb-Scargle periodograms of the time series, with horizontal solid, dashed and dotted lines marking the 10%, 1% and 0.1% FAP thresholds.

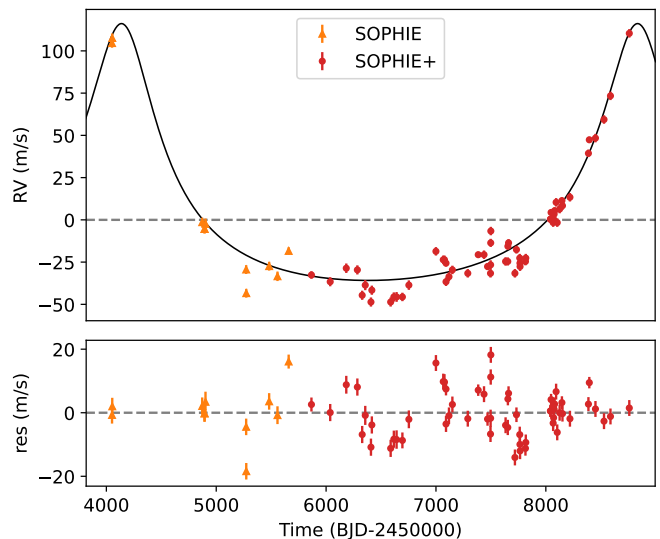


Fig. 4. Radial velocity orbital fit for planet HD 57625 b. *Top panel:* best-fit single-Keplerian solution is shown as a black curve over the SOPHIE (orange triangles) and SOPHIE+ (red circles) archival data. *Bottom panel:* post-fit residual radial velocities.

uncertainty of 2.5 m s^{-1} . In Fig. 3 we show the time series and GLS periodograms for the SOPHIE and SOPHIE+ RVs, the one-Keplerian solution residuals and the activity indexes derived and discussed in Sect. 2; all time series are also listed in Table 2. The RV time series exhibits a peak-to-valley variation of 151 m s^{-1} and a clear Keplerian behaviour hinting at the presence of a moderate-to-high eccentricity companion with a GLS-derived period longer than 4500 d. While it must be noted that the available public data fail to fully cover the entirety of the RV oscillation, the current coverage allow for a significant portion of the oscillation to be detected and analysed. We note, as mentioned in Sect. 2, that no activity index shows significant correlation with the RV time series, with all indexes having Pearson correlation coefficient $|\rho| < 0.27$ with the exceptions of FWHM ($\rho = -0.54$) and S_{MW} ($\rho = 0.49$) having moderate correlation. However, we note that both time series and periodogram of these indexes hint at different periodicities than the $>4500 \text{ d}$ observed in the RVs, with the FWHM periodogram peaking at $\sim 3900 \text{ d}$ and the S_{MW} variation not having gone through a full cycle over the observational time span of 4708 d and therefore strongly suggesting a periodicity much longer than that observed in the RVs.

Although we noted in Sect. 2 the presence of a $\sim 0.2 M_{\odot}$ stellar companion at a separation of $10''$, we exclude a binary origin for the observed RV variation. With a projected orbital separation of $\sim 440 \text{ au}$, the orbital period of the secondary around the primary would be of $\sim 8.5 \cdot 10^3 \text{ a}$, an exceedingly long period compared to the observed RV oscillation. Additionally, we can follow Torres (1999) and estimate the acceleration $d(RV)/dt$ caused by the secondary on the primary as:

$$\frac{d(RV)}{dt} = G \frac{M_B}{a^2(1-e)} \frac{(1 + \cos \nu) \sin(\nu + \omega) \sin i}{(1 + \cos E)(1 - e \cos E)} \quad (1)$$

being $a = a_A(M_A + M_B)/M_B$ the semi-major axis of the relative orbit, ν is the true anomaly, i is the mutual inclination, and E is the eccentric anomaly. As we lack any estimate of the binary system orbital elements except the aforementioned separation and mass estimates, we generated 10^5 possible combinations of orbital elements (e, ν, ω, E, i) . We obtain a maximum possible

Table 3. RV-only best-fit orbital solution for HD 57625 b.

| Parameter | Priors | Best-fit values |
|------------------------------------------|---------------------------------|---------------------------|
| P_b (d) | $\mathcal{U}(2000, 10000)$ | 4851^{+413}_{-178} |
| K_b (m s $^{-1}$) | $\mathcal{U}(0, +\infty)$ | $78.94^{+19.87}_{-5.85}$ |
| $\sqrt{e_b} \sin \omega_b$ | $\mathcal{U}(-1, 1)$ | $0.006^{+0.072}_{-0.058}$ |
| $\sqrt{e_b} \cos \omega_b$ | $\mathcal{U}(-1, 1)$ | $0.723^{+0.026}_{-0.028}$ |
| λ_0 (deg) | $\mathcal{U}(0, 360)$ | $47.82^{+9.44}_{-17.68}$ |
| ω_b (deg) | derived | $0.46^{+5.54}_{-4.70}$ |
| e_b | derived | 0.52 ± 0.04 |
| $M_b \sin i$ (M_{Jup}) | derived | $5.79^{+1.71}_{-0.63}$ |
| a_b (au) | derived | $5.71^{+0.33}_{-0.21}$ |
| γ_{SOPHIE} (m s $^{-1}$) | $\mathcal{U}(-\infty, +\infty)$ | $14.41^{+9.55}_{-5.37}$ |
| $\gamma_{\text{SOPHIE+}}$ (m s $^{-1}$) | $\mathcal{U}(-\infty, +\infty)$ | $22.62^{+11.09}_{-5.17}$ |
| j_{SOPHIE} (m s $^{-1}$) | $\mathcal{U}(0, +\infty)$ | $9.55^{+3.38}_{-2.19}$ |
| $j_{\text{SOPHIE+}}$ (m s $^{-1}$) | $\mathcal{U}(0, +\infty)$ | $6.85^{+0.81}_{-0.70}$ |

variation of only ~ 0.19 m s $^{-1}$ over the 12.5 a SOPHIE baseline, an exceedingly lower value than the 151 m s $^{-1}$ variation observed in the archival data.

We therefore search for the best-fit orbital solution using the Python tool PyORBIT⁶ (Malavolta et al. 2016, 2018), a package for the Markov chain Monte Carlo (MCMC) modeling of RV and activity indexes time series based on the optimization algorithm PyDE (Storn & Price 1997) and the MCMC sampler emcee (Foreman-Mackey et al. 2013). The nine free parameters we fit for are orbital period P , semi-amplitude K , mean longitude λ_0 , $\sqrt{e_b} \sin \omega_b$, $\sqrt{e_b} \cos \omega_b$, and finally a zero-point radial velocity term γ and an uncorrelated stellar jitter term j each for SOPHIE and SOPHIE+ datasets.

We find a best-fit Keplerian solution (see Fig. 4 and Table 3) with orbital period 4851^{+413}_{-178} d, semi-amplitude $78.94^{+19.87}_{-5.85}$ m s $^{-1}$ and eccentricity 0.52 ± 0.04 . Using the host star mass value of $1.040^{+0.078}_{-0.080} M_{\odot}$ we obtained in Sect. 2, we derive a companion minimum mass of $5.79^{+1.71}_{-0.63} M_{\text{Jup}}$ and semi-major axis of $5.71^{+0.33}_{-0.21}$ au. We immediately note that both P and especially K of the detected companion upper limits are somewhat unconstrained, with upper relative uncertainties of 8.5% and 25%, a clear result of the aforementioned incomplete orbital coverage of the available SOPHIE public data. Indeed, not only the best-fit orbital period is close to the observational baseline of 4708 d, but the available RV measurements are characterized by a lack of full sampling over the maximum portion of the companion-induced oscillation, therefore limiting a full characterization of some orbital elements of the planetary companion with the exclusive use of currently available RV observations. Finally, the residual time series has a weighted root mean square (w.r.m.s.) of 7 m s $^{-1}$, has no significant correlation with any of the activity indexes analysed ($|\rho| < 0.2$) and exhibits a non-significant principal peak at ~ 1300 d with a 6% FAP in its GLS periodogram (see second row of Fig. 3).

As such, the HD 57625 system calls for further follow-up RV observations to fully constrain the orbital parameters of planet b. However, as we will show in the following Sections, the simultaneous usage of astrometric and imaging measurements can provide additional constrains to the RV-only system characterization.

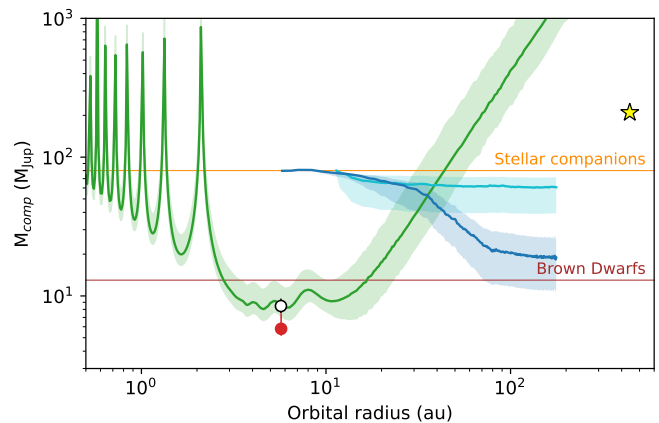


Fig. 5. Proper motion anomaly sensitivity curve for HD 57625. The dark green curve shows the PMA-compatible companion masses as a function of orbital separations, the shaded region corresponding to the 1σ uncertainty range. The blue and cyan curves represent the SHARK-NIR and LMIRCcam mass limits as in Fig. 2. Horizontal lines indicate the brown dwarf (brown) and stellar mass (orange) thresholds. The positions of HD 57625 b as obtained by the RV-only fit and by the joint RV and PMA fit are shown as a red and white circle, respectively, while the distant stellar companion is shown as a yellow star.

5. Astrometry analysis

As previously discussed, one of the main hints of the presence of a companion orbiting HD 57625 is the highly significant variation in proper motion measurements between the Hipparcos and Gaia DR3 epochs, which Kervella et al. (2022) reports as having a SNR of 11.04. Assuming a $1.16 \pm 0.06 M_{\odot}$ mass for the host star, the catalog estimates a companion dynamical mass of $11.18 M_{\text{Jup}}$ at a separation of 3 au, of $8.91 M_{\text{Jup}}$ at 5 au, of $9.33 M_{\text{Jup}}$ at 10 au and of $37.45 M_{\text{Jup}}$ at 30 au, indicating that the observed PMA is compatible with either a planetary-mass companion at short-to-wide separations or a brown dwarf or stellar companion at larger separations.

In Fig. 5, following the method detailed in Kervella et al. (2022), the companion masses compatible with the observed astrometric acceleration is plotted as a function of possible orbital separations. We note that the distant stellar companion mentioned in Sect. 2, shown in Fig 5 as a yellow star, is not compatible with the observed PMA, as a companion with its assumed mass of $\sim 0.2 M_{\odot}$ would be responsible for the reported acceleration only at an orbital separation of ~ 70 au, much closer than the projected separation of 440 au of the known stellar companion.

On the other hand, the RV-detected companion with minimum mass $5.79^{+1.71}_{-0.63} M_{\text{Jup}}$ and semi-major axis $5.71^{+0.33}_{-0.21}$ au discussed in Sect. 4 (shown in Fig. 5 as a red circle) is compatible within 2σ with the observed PMA. The same Figure additionally shows that only planetary-mass companions satisfactorily explain the observed PMA within the orbital separation compatible with the RV signal detected in the SOPHIE public data, strongly suggesting a planetary true mass companion to be the origin of both the RV and PMA signals.

To provide a more complete characterization of the orbital elements of HD 57625 b, and more specifically a precise value of dynamical mass, we used the Python code orvara (Brandt et al. 2021), an MCMC code designed to fit Keplerian orbits to any combination of proper motion variations, absolute and relative astrometry, and radial velocities to obtain precise dynamical masses and orbital elements. More specifically, orvara is de-

⁶ <https://github.com/LucaMalavolta/PyORBIT>

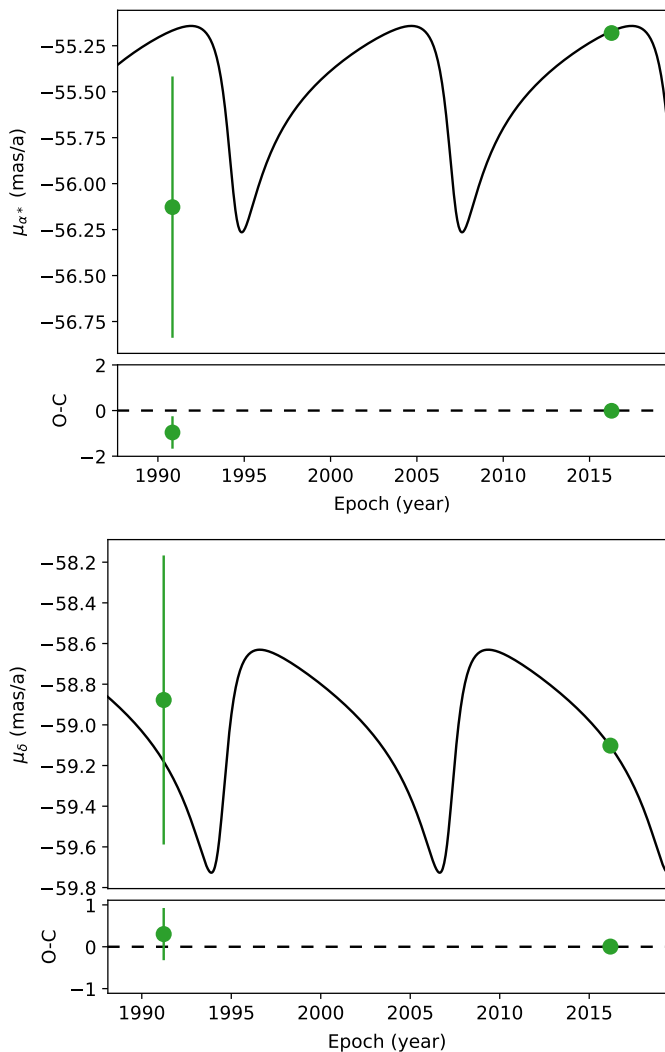


Fig. 6. Observed and fitted proper motions in right ascension (*top panel*) and declination (*bottom panel*). The best-fit orbit obtained by the joint RV and PMA fit is shown as a black curve, with the proper motion measurements from Hipparcos and Gaia EDR3 shown as green circles.

signed to use the PMA computed and reported in the Hipparcos-Gaia Catalog of Accelerations (HGCA, Brandt 2018, 2021), in which the Hipparcos and Gaia EDR3 catalogues have been cross-calibrated to account for systematics and shift all proper motions in the Gaia EDR3.

The best-fit orbital parameters obtained by the joint RV-PMA fit are listed in Table 4, with best-fit proper motion anomaly curves shown in Fig. 6 and relative astrometric orbit with predicted positions at selected epochs for the planetary companion shown in Fig. 7. This solution characterizes HD 57625 b as having an orbital period of 4843^{+306}_{-167} d, eccentricity of $0.52^{+0.04}_{-0.03}$, inclination of $43.82^{+14.30}_{-7.22}$ deg and dynamical mass of $8.43^{+1.1}_{-0.91} M_{\text{Jup}}$.

We show the companion’s position in the mass-separation parameter space as a white circle compared with the PMA sensitivity curve in Fig. 5, highlighting the solution’s agreement with the observed PMA. We note that the orbital period derived from the joint RV-PMA solution is compatible and more precise than the RV-only one obtained in Sect. 4, and the same applies to the companion dynamical mass which additionally lies firmly below

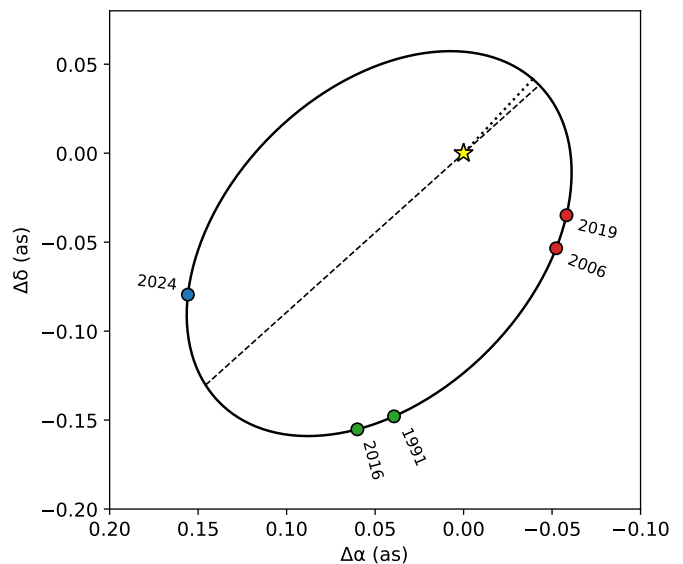


Fig. 7. Relative astrometric orbit and selected predicted position for HD 57625 b. The position of the host star is marked by a yellow star, with a dashed line representing the line of nodes and a dotted line connecting the host star to periastron. Coloured circles mark the predicted positions of the planetary companion at the epoch of our imaging observation (2024, blue), at the starting and final epochs of available RVs (2006 and 2019, red) and at the reference epochs for Hipparcos and Gaia DR3 (1991 and 2024, green)

Table 4. Joint RV and PMA best-fit orbital solution for HD 57625 b.

| Parameter | Priors | Best-fit values |
|--------------------------------------------|-------------------------------|---------------------------|
| M_b (M_{Jup}) | $1/M$ (log-flat) | $8.43^{+1.10}_{-0.91}$ |
| a_b (au) | $1/a$ (log-flat) | $5.70^{+0.14}_{-0.13}$ |
| $\sqrt{e_b} \sin \omega_b$ | $\mathcal{U}(-1, 1)$ | $0.008^{+0.068}_{-0.056}$ |
| $\sqrt{e_b} \cos \omega_b$ | $\mathcal{U}(-1, 1)$ | $0.720^{+0.023}_{-0.026}$ |
| i_b (deg) | $\cos i, \mathcal{U}(0, 180)$ | $43.82^{+14.30}_{-7.22}$ |
| λ_0 (deg) | $\mathcal{U}(0, 360)$ | $89.4^{+7.1}_{-6.1}$ |
| Ω_b (deg) | $\mathcal{U}(0, 360)$ | 301^{+13}_{-40} |
| P_b (d) | derived | 4843^{+306}_{-167} |
| ω_b (deg) | derived | $9.2^{+349}_{-7.2}$ |
| e_b | derived | $0.52^{+0.04}_{-0.03}$ |
| j_{SOPHIE} (m s^{-1}) | $1/j$ (log-flat) | $8.8^{+2.9}_{-2.0}$ |
| $j_{\text{SOPHIE+}}$ (m s^{-1}) | $1/j$ (log-flat) | $6.76^{+0.78}_{-0.68}$ |

the traditionally assumed $13 M_{\text{Jup}}$ deuterium-burning threshold, confirming the planetary nature of HD 57625 b.

6. Detection completeness

In addition to allowing the detection of the planetary companion HD 57625 b, the imaging, RV and PMA data analysed in the previous Sections can be further used to assess the detection completeness of the datasets. By doing so, we can identify the full-completeness regions in the mass-separation parameter space in which the available data can exclude the presence of additional companions or, on the contrary, the low-completeness regions in which additional companions could, in principle, be detected by follow-up observations.

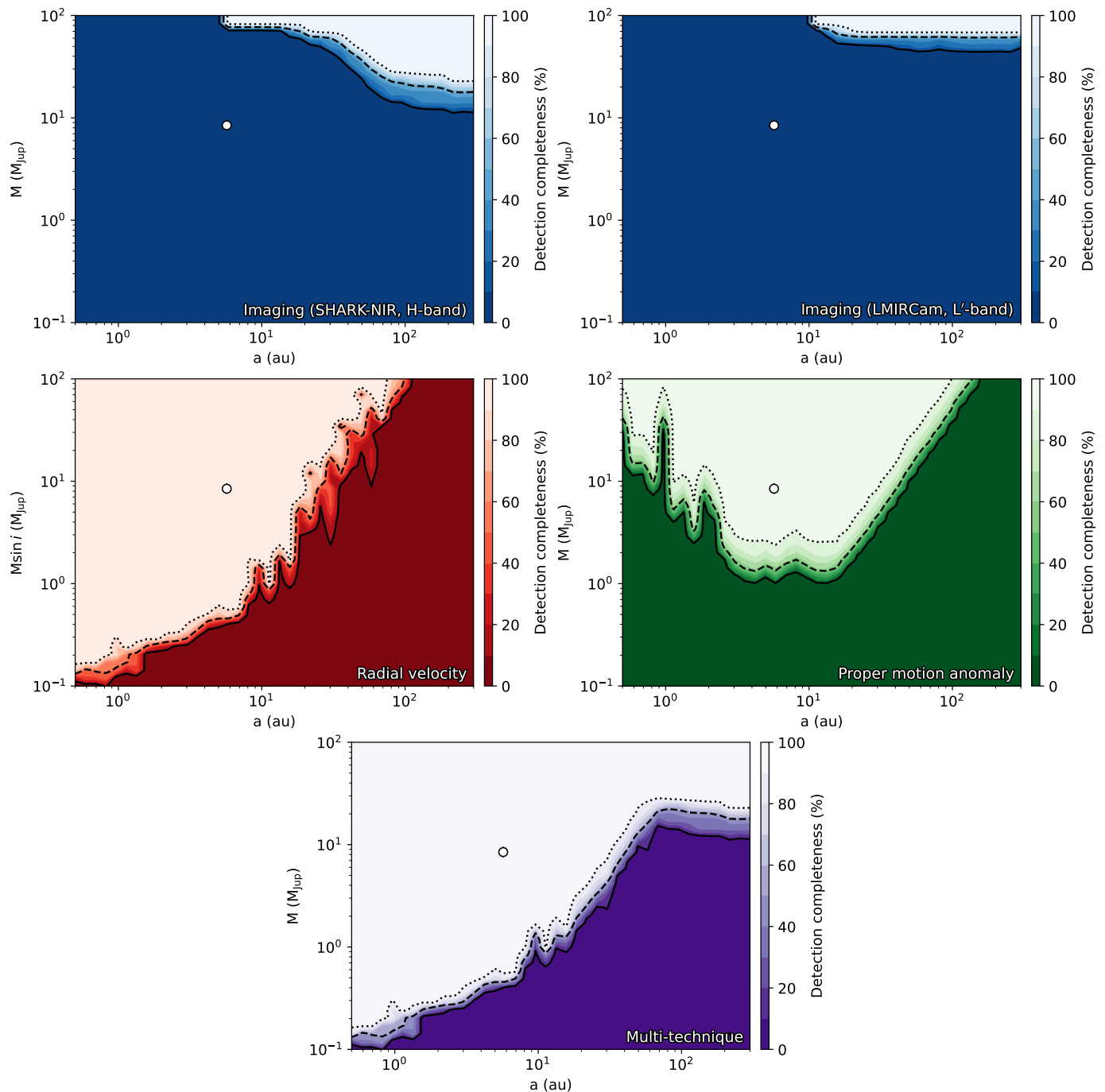


Fig. 8. Detection completeness maps for the imaging (blue, *top row*), radial velocity (red, *middle left panel*), proper motion anomaly data (green, *middle right panel*) discussed in this work, as well as the multi-technique global map (purple, *bottom panel*). In all panels, the solid, dashed and dotted curves identify the 10%, 50% and 100% detection completeness thresholds, a white circle marks the position of the detected planetary companion as obtained by the joint RV and PMa fit.

In order to do so, we follow an injection and retrieval scheme in which synthetic companions are injected into the available datasets and subject to statistical tests to assess their detectability. We use a Python code we developed to assess the detection completeness of RV time series analysed in previous works (Barbato et al. 2018, 2019, 2023; Matthews et al. 2023; Gratton et al. 2024; Mesa et al. 2024), now expanded to also be used on imaging and astrometric data in order to produce multi-technique detection completeness maps.

We explore a grid of 40×40 companion masses and orbital separations, respectively ranging from 0.1 to $100 M_{\text{Jup}}$ (consid-

ering true mass M for imaging and PMa data, and minimum masses $M \sin i$ for RV data) and from 0.5 to 300 au. This wide parameter space spans a large variety of companion categories, from close-in giant planets to wide-orbit low-mass stellar companions, allowing both the investigation of different possible companions and the showcasing of each datasets discovery space and synergic interplay. For each mass-separation realization, we generate 10^3 sets of randomly drawn values of e , ω , Ω , λ_0 , i and stellar age used to compute as many synthetic H and L'-band contrast, RV time series and PMa signals corresponding to the injected companion. We note that the age values are drawn

from a uniform distribution between the lower and upper values of stellar age derived for HD 57625 in Sect. 2, in order to account for this parameter uncertainty and the dependence of H-band injected companion emission we compute using the AMES-COND models, and therefore of the detecting capability of imaging observations, as a function of the system age.

We then perform a statistical test to assess the detectability of each of the $1.6 \cdot 10^6$ synthetic companions with each of the considered techniques, considering the injected signal detected with imaging if the computed contrast is higher than the measured non-detection contrast curve at the corresponding separation (see Fig. 2), with radial velocity if the injected companion produces a periodogram peak with $\text{FAP} \leq 10^{-3}$ and by astrometry if the injected proper motion anomaly has $\text{SNR} \geq 3$. Finally, for each mass-separation realization we compute the detection completeness as the ratio between detectable injected signals and total injections. The detection completeness maps thusly obtained for all techniques considered in this work are shown in Fig. 8, the position of the detected exoplanet marked by a white circle.

Starting with imaging (top row), it is immediate to note that the detection completeness of our SHARK-NIR H-band observation (left panel) is limited for lower orbital separations by its IWA of 120 mas, corresponding to 5.30 au given the nominal stellar distance of 44.24 pc. Above this lower limit on separation, we achieve full completeness only for stellar companions ($>80 M_{\text{Jup}}$) at all separations explored, and for massive brown dwarfs ($>30 M_{\text{Jup}}$) beyond 80 au. Our LMIRCam L' -band observation (right panel) is found to be more limited for close-in companions, due to its higher IWA of 246 mas corresponding to 10.88 au for our star, and provides full completeness only for outer stellar ($>80 M_{\text{Jup}}$) companions. While the planetary companion detected with radial velocities and proper motion anomaly remains firmly beyond the detection capabilities of both SHARK-NIR and LMIRCam, by virtue of its relatively low mass and orbital separation comparable and lower than SHARK-NIR and LMIRCam IWA respectively, our observations allow to robustly exclude the presence of massive brown dwarfs or stellar companions at all separations of interest, once again stressing the planetary nature of the detected RV and PMA signal. Additionally, we note the presence of significant discovery space for wide orbit giant planetary companions for follow-up deep imaging observations.

Considering instead radial velocity (middle left panel), the public SOPHIE data provide full detection completeness above minimum masses of $0.2 M_{\text{Jup}}$ within 1 au, above $1.5 M_{\text{Jup}}$ within 10 au and finally above $20 M_{\text{Jup}}$ below 30 au, allowing us to exclude the presence of additional companions in the system in these regions in the parameter space. On the other hand, the available RV data is still blind to the presence of less massive giant exoplanets on wide orbits, such as companions with $M \sin i < 0.2 M_{\text{Jup}}$ beyond 1.5 au, $<1 M_{\text{Jup}}$ beyond 10 au and $<10 M_{\text{Jup}}$ beyond 40 au. Therefore, follow-up RV observations still have some significant discovery space available for the detection of long-period giant planets, as well as lower-mass companions on a large variety of orbits.

Finally, the astrometry detection map (middle right panel) shows that the Hipparcos-Gaia proper motion anomalies precision provide full completeness for massive companions, such as those with true mass larger than $4 M_{\text{Jup}}$ between 2.5 and 15 au, as well as larger than $30 M_{\text{Jup}}$ below 50 au, allowing us to further exclude the presence of additional massive companions in the system within these orbital ranges. On the other hand, a significant portion of giant planet mass regime remains below the current detection capabilities of the PMA measurements for

HD 57625, with no sub-Jovian companion being detectable at any of the orbital separations explored, allowing for significant exoplanetary discovery space with full astrometric orbit measurements in future Gaia releases.

To conclude, we additionally shown in the bottom panel of Fig. 8 a multi-technique global detection completeness map, obtained by considering each injected companion detected by at least one of the datasets studied so far. From this map is evident how the multi-technique observations of HD 57625 allow to compensate each technique's weaknesses and provide a rather complete view of the system, with RV data probing the inner, low-mass region of the parameter space to which the other techniques are blind, PMA providing completeness for intermediate-to-large separation giant companions and imaging probing the more massive and outer regions of the system, once again highlighting the importance of multi-technique observations and analysis for the characterization of planetary systems.

7. Discussion and conclusions

In this work we reported the detection and characterization of HD 57625 b, the giant planetary companion responsible for the astrometric acceleration of its host star, via a synergic analysis of imaging, radial velocity and astrometric datasets. To investigate the observed significant proper motion anomaly between Hipparcos and Gaia DR3, we performed high-contrast H-band observations with SHARK-NIR, the near-infrared camera recently installed at the Large Binocular Telescope, in parallel with LMIRCam in L' , resulting in a non-detection that allowed us to confirm a substellar nature for the unseen companion causing the observed acceleration.

By jointly analysing public archival SOPHIE radial velocity time series and the Hipparcos-Gaia DR3 proper motion anomaly measurements we further confirm the planetary nature of the companion, characterize its orbit as well as determining its true mass even facing incomplete orbital coverage by the available radial velocity measurements. We find HD 57625 b to be a giant exoplanet with a true mass of $8.43^{+1.1}_{-0.91} M_{\text{Jup}}$ on a $5.70^{+0.14}_{-0.13}$ au orbit with a relatively high eccentricity of $0.52^{+0.04}_{-0.03}$. To further analyse the planetary system and fuel future observations, we additionally performed a multi-technique detection completeness assessment, finding significant yet-unexplored discovery space for additional outer giant and inner low-mass companions, as well as underlying the importance of synergic multi-technique analysis in fully characterizing exoplanetary systems.

A noteworthy characteristic of HD 57625 b is its moderate-to-high value of orbital eccentricity, which for giant planets usually interpreted as the result of either Kozai-Lidov effects (Kozai 1962; Innanen et al. 1997; Wu & Murray 2003), in which the planetary eccentricity growth is driven by secular interactions with a distant stellar or brown dwarf companion, or planet-planet scattering (Weidenschilling & Marzari 1996; Chambers et al. 1996; Raymond et al. 2009), in which gravitational instability in multi-planet systems leads to repeated orbital encounters often resulting in multiple surviving planetary companions with high eccentricities.

While our multi-technique detection completeness assessment proves that yet-undiscovered outer giant planetary companions could still be present in the HD 57625 system, the lack of inner massive companions and especially the presence of the wide-orbit stellar companion 2MASS J07251770+5634002 (Gaia DR3 989016790859521280) suggest a Kozai-driven origin for the observed eccentricity of HD 57625 b. Indeed, follow-

ing Ford et al. (2000) and Takeda & Rasio (2005) we can estimate the timescale for Kozai-driven eccentricity modulation as:

$$P_{\text{Kozai}} \approx P_b \frac{M_A + M_b}{M_B} \left(\frac{a_B}{a_b} \right)^3 (1 - e_B^2)^{3/2} \quad (2)$$

with the indexes b, A and B referring to the planetary companion, the primary and secondary component of the binary system, respectively. As we have estimates of $M_B \sim 0.2 M_\odot$ and $a_B \sim 440$ au for the distant stellar companion but no assessment on its orbital eccentricity, we consider extreme values of 0 and 0.9 for e_B . Accounting for the uncertainties in host star and planetary companion parameters, we obtain values of P_{Kozai} ranging from 26 to 39 Ma assuming $e_B = 0$ and from 2 to 3 Ma for $e_B = 0.9$. As these timescales are considerably lower than the host star age of $4.8^{+3.7}_{-2.9}$ Ga, it is clear that the planetary system has undergone a large number of oscillation cycles, and as such we identify Kozai interaction as a likely responsible for the planetary companion eccentricity. However, in the absence of information on the stellar companion orbital orientation, we are currently unable to determine whether the planet-secondary relative orbital inclination is higher than the threshold value of 39.2° needed to incite Kozai oscillations. While in principle the combination of proper motion vector and radial velocity measurements for the wide-orbit stellar companion can be used to provide a characterization of its orbital inclination, no value of radial velocity is available in Gaia DR3 or in previous literature. Furthermore, the stellar companion is not a part of the Hipparcos catalog, preventing any orbital characterization using PMa. As such, the relative orbital inclination of HD 57625 b and 2MASS J07251770+5634002 is impossible to determine, although future Gaia DRs could provide additional measurements and help shed light on the system dynamical history.

Finally, we highlight that HD 57625 b joins the population of long-period giant planetary companions having true mass value determined via the synergic usage of multiple detection methods. As of the time of writing, only a few tens of such exoplanets are known, most of which have had their dynamical mass characterized only in recent years thanks to the usage of Gaia astrometric measurements and the growing multi-technique analysis approach in exoplanetology. As such, many studies assessing exoplanetary occurrence rates often characterize detected massive companions based on minimum mass estimates or the presence of long-term RV trends (see e.g. Bryan et al. 2019; Rosenthal et al. 2022) and therefore are highly dependant on the inherent planetary mass degeneracy in the absence of additional constraints. Therefore, this small but growing sample of outer giant exoplanets with true mass determination represents an important asset in exoplanetology, and the growing multi-technique exoplanetology approach as well as the future Gaia data releases and astrometric solutions will continue to prove essential in exploring the observed variety of exoplanetary system architectures, as well as furthering our understanding of the formation and dynamical evolution processes that shaped such variety.

Acknowledgements. The authors wish to thank the anonymous referee for their useful comments. We thank Tom Herbst from MPIA-Heidelberg and the LINC-NIRVANA team for sharing part of their instrument control SW to operate the motorized axis of SHARK-NIR. We also express our appreciation to NASA and Marcia Rieke, the Principal Investigator of JWST/NIRCam, for granting us the opportunity to utilize one of the NIRCam spare detectors as the primary detector for the SHARK-NIR scientific camera. Observations have benefited from the use of ALTA Center (alta.arcetri.inaf.it) forecasts performed with the Astro-Meso-Nh model. Initialization data of the ALTA automatic forecast system come from the General Circulation Model (HRES) of the European Centre for Medium Range Weather Forecasts. The LBT is an international collaboration among institutions in the United States, Italy and Germany. The LBT

Corporation partners are: The University of Arizona on behalf of the Arizona university system; Istituto Nazionale di Astrofisica, Italy; LBT Beteiligungsgesellschaft, Germany, representing the Max Planck Society, the Astrophysical Institute Potsdam, and Heidelberg University; The Ohio State University; The Research Corporation, on behalf of The University of Notre Dame, University of Minnesota and University of Virginia. DB and AR wish to thank J. Gomes da Silva for his great availability and invaluable support in adapting and applying ACTIN2 to this work. AR acknowledges support by the Fondazione ICSC, Spoke 3 Astrophysics and Cosmos Observations. National Recovery and Resilience Plan (Piano Nazionale di Ripresa e Resilienza, PNRR) Project ID CN_00000013 "Italian Research Center on High-Performance Computing, Big Data and Quantum Computing" funded by MUR Missione 4 Componente 2 Investimento 1.4: Potenziamento strutture di ricerca e creazione di "campioni nazionali di R&S (M4C2-19)" - Next Generation EU (NGEU). This work has made use of data retrieved from the SOPHIE archive at Observatoire de Haute-Provence (OHP), available at atlas.obs-hp.fr/sophie. This work has made use of data from the European Space Agency (ESA) mission *Gaia* (<https://www.cosmos.esa.int/gaia>), processed by the *Gaia* Data Processing and Analysis Consortium (DPAC, <https://www.cosmos.esa.int/web/gaia/dpac/consortium>). Funding for the DPAC has been provided by national institutions, in particular, the institutions participating in the *Gaia* Multilateral Agreement. This research has made extensive use of the NASA-ADS, SIMBAD and Vizier databases, operated at CDS, Strasbourg, France.

References

- Allard, F., Guillot, T., Ludwig, H.-G., et al. 2003, in IAU Symposium, Vol. 211, Brown Dwarfs, ed. E. Martín, 325
- Amara, A. & Quanz, S. P. 2012, MNRAS, 427, 948
- Barbato, D., Farinato, J., Baruffolo, A., et al. 2024, in Ground-based and Airborne Instrumentation for Astronomy X, ed. J. J. Bryant, K. Motohara, & J. R. D. Vernet, Vol. 13096, International Society for Optics and Photonics (SPIE), 130961W
- Barbato, D., Ségransan, D., Udry, S., et al. 2023, A&A, 674, A114
- Barbato, D., Sozzetti, A., Biazzo, K., et al. 2019, A&A, 621, A110
- Barbato, D., Sozzetti, A., Desidera, S., et al. 2018, A&A, 615, A175
- Bonavita, M., Fontanive, C., Gratton, R., et al. 2022, MNRAS, 513, 5588
- Bouchy, F., Díaz, R. F., Hébrard, G., et al. 2013, A&A, 549, A49
- Brandt, T. D. 2018, ApJS, 239, 31
- Brandt, T. D. 2021, ApJS, 254, 42
- Brandt, T. D., Dupuy, T. J., Li, Y., et al. 2021, AJ, 162, 186
- Bryan, M. L., Knutson, H. A., Lee, E. J., et al. 2019, AJ, 157, 52
- Calissendorff, P. & Janson, M. 2018, A&A, 615, A149
- Cannon, A. J. & Pickering, E. C. 1993, VizieR Online Data Catalog: Henry Draper Catalogue and Extension (Cannon+ 1918-1924; ADC 1989), VizieR On-line Data Catalog: III/135A. Originally published in: Harv. Ann. 91-100 (1918-1924)
- Carolo, E., Vassallo, D., Farinato, J., et al. 2018, in Society of Photo-Optical Instrumentation Engineers (SPIE) Conference Series, Vol. 10701, Optical and Infrared Interferometry and Imaging VI, ed. M. J. Creech-Eakman, P. G. Tuthill, & A. Mérand, 107012B
- Chambers, J. E., Wetherill, G. W., & Boss, A. P. 1996, Icarus, 119, 261
- Choi, J., Dotter, A., Conroy, C., et al. 2016, ApJ, 823, 102
- Currie, T., Brandt, T. D., Kuzuhara, M., et al. 2020, ApJ, 904, L25
- Cutri, R. M., Skrutskie, M. F., van Dyk, S., et al. 2003, VizieR Online Data Catalog: 2MASS All-Sky Catalog of Point Sources (Cutri+ 2003), VizieR On-line Data Catalog: II/246. Originally published in: 2003yCat.2246...0C
- Cutri, R. M., Wright, E. L., Conrow, T., et al. 2021, VizieR Online Data Catalog, II/328
- De Rosa, R. J., Nielsen, E. L., Wahhaj, Z., et al. 2023, A&A, 672, A94
- Doelman, D. S., Snik, F., Por, E. H., et al. 2021, Appl. Opt., 60, D52
- Dotter, A. 2016, ApJS, 222, 8
- Eastman, J. D., Rodriguez, J. E., Agol, E., et al. 2019, arXiv e-prints, arXiv:1907.09480
- Farinato, J., Baruffolo, A., Bergomi, M., et al. 2022, in Society of Photo-Optical Instrumentation Engineers (SPIE) Conference Series, Vol. 12185, Adaptive Optics Systems VIII, ed. L. Schreiber, D. Schmidt, & E. Vernet, 1218522
- Farinato, J., Di Filippo, S., Baruffolo, A., et al. 2023, in Adaptive Optics for Extremely Large Telescopes (AO4ELT7), 68
- Ford, E. B., Kozinsky, B., & Rasio, F. A. 2000, ApJ, 535, 385
- Foreman-Mackey, D., Hogg, D. W., Lang, D., & Goodman, J. 2013, PASP, 125, 306
- Franson, K., Bowler, B. P., Zhou, Y., et al. 2023, ApJ, 950, L19
- Gaia Collaboration, Brown, A. G. A., Vallenari, A., et al. 2018, A&A, 616, A1
- Gaia Collaboration, Prusti, T., de Bruijne, J. H. J., et al. 2016, A&A, 595, A1
- Gaia Collaboration, Smart, R. L., Sarro, L. M., et al. 2021, A&A, 649, A6
- Gaia Collaboration, Vallenari, A., Brown, A. G. A., et al. 2023, A&A, 674, A1

- Galicher, R., Marois, C., Macintosh, B., et al. 2016, *A&A*, 594, A63
- Głębocki, R. & Gnaciński, P. 2005, in *ESA Special Publication*, Vol. 560, 13th Cambridge Workshop on Cool Stars, Stellar Systems and the Sun, ed. F. Favata, G. A. J. Hussain, & B. Battrick, 571
- Gomes da Silva, J., Figueira, P., Santos, N., & Faria, J. 2018, *The Journal of Open Source Software*, 3, 667
- Gomes da Silva, J., Santos, N. C., Adibekyan, V., et al. 2021, *A&A*, 646, A77
- Gratton, R., Bonavita, M., Mesa, D., et al. 2024, *A&A*, 685, A119
- Haffert, S. Y., Bohn, A. J., de Boer, J., et al. 2019, *Nature Astronomy*, 3, 749
- Hinkley, S., Lacour, S., Marleau, G. D., et al. 2023, *A&A*, 671, L5
- Høg, E., Fabricius, C., Makarov, V. V., et al. 2000, *A&A*, 355, L27
- Innanen, K. A., Zheng, J. Q., Mikkola, S., & Valtonen, M. J. 1997, *AJ*, 113, 1915
- Keppler, M., Benisty, M., Müller, A., et al. 2018, *A&A*, 617, A44
- Kervella, P., Arenou, F., & Thévenin, F. 2022, *A&A*, 657, A7
- Kozai, Y. 1962, *AJ*, 67, 591
- Kuzuhara, M., Tamura, M., Kudo, T., et al. 2013, *ApJ*, 774, 11
- Leisenring, J. M., Skrutskie, M. F., Hinz, P. M., et al. 2012, in *Ground-based and Airborne Instrumentation for Astronomy IV*, ed. I. S. McLean, S. K. Ramsay, & H. Takami, Vol. 8446, International Society for Optics and Photonics (SPIE), 84464F
- Li, Y. & Ezzeddine, R. 2023, *AJ*, 165, 145
- Macintosh, B., Graham, J. R., Barman, T., et al. 2015, *Science*, 350, 64
- Malavolta, L., Mayo, A. W., Loudon, T., et al. 2018, *AJ*, 155, 107
- Malavolta, L., Nascimbeni, V., Piotto, G., et al. 2016, *A&A*, 588, A118
- Mamajek, E. E. & Hillenbrand, L. A. 2008, *ApJ*, 687, 1264
- Marafatto, L., Carolo, E., Umbriaco, G., et al. 2022, in *Society of Photo-Optical Instrumentation Engineers (SPIE) Conference Series*, Vol. 12184, *Ground-based and Airborne Instrumentation for Astronomy IX*, ed. C. J. Evans, J. J. Bryant, & K. Motohara, 121843V
- Marois, C., Lafrenière, D., Doyon, R., Macintosh, B., & Nadeau, D. 2006, *ApJ*, 641, 556
- Marois, C., Macintosh, B., Barman, T., et al. 2008, *Science*, 322, 1348
- Marois, C., Zuckerman, B., Konopacky, Q. M., Macintosh, B., & Barman, T. 2010, *Nature*, 468, 1080
- Matthews, E. C., Bonnefoy, M., Xie, C., et al. 2023, *A&A*, 679, A58
- Matthews, E. C., Carter, A. L., Pathak, P., et al. 2024, *Nature*, 633, 789
- Mesa, D., Bonavita, M., Benatti, S., et al. 2022, *A&A*, 665, A73
- Mesa, D., Gratton, R., D’Orazi, V., et al. 2024, *arXiv e-prints*, arXiv:2412.04171
- Mesa, D., Gratton, R., Kervella, P., et al. 2023, *A&A*, 672, A93
- Meyer, M. R., Amara, A., Reggiani, M., & Quanz, S. P. 2018, *A&A*, 612, L3
- Moultaka, J., Ilovaisky, S. A., Prugniel, P., & Soubiran, C. 2004, *PASP*, 116, 693
- Müller, A., Keppler, M., Henning, T., et al. 2018, *A&A*, 617, L2
- Nielsen, E. L., De Rosa, R. J., Macintosh, B., et al. 2019, *AJ*, 158, 13
- Nowak, M., Lacour, S., Lagrange, A. M., et al. 2020, *A&A*, 642, L2
- Noyes, R. W., Hartmann, L. W., Baliunas, S. L., Duncan, D. K., & Vaughan, A. H. 1984, *ApJ*, 279, 763
- Pecaut, M. J. & Mamajek, E. E. 2013, *ApJS*, 208, 9
- Pedichini, F., Piazzesi, R., Viavattene, G., et al. 2022, in *Adaptive Optics Systems VIII*, ed. L. Schreiber, D. Schmidt, & E. Vernet, Vol. 12185, International Society for Optics and Photonics (SPIE), 121856Q
- Perruchot, S., Kohler, D., Bouchy, F., et al. 2008, in *Society of Photo-Optical Instrumentation Engineers (SPIE) Conference Series*, Vol. 7014, *Ground-based and Airborne Instrumentation for Astronomy II*, ed. I. S. McLean & M. M. Casali, 70140J
- Pinna, E., Esposito, S., Hinz, P., et al. 2016, in *Adaptive Optics Systems V*, ed. E. Marchetti, L. M. Close, & J.-P. Véran, Vol. 9909, International Society for Optics and Photonics (SPIE), 99093V
- Pinna, E., Rossi, F., Agapito, G., et al. 2023, in *Adaptive Optics for Extremely Large Telescopes (AO4ELT7)*, 80
- Raymond, S. N., Barnes, R., Veras, D., et al. 2009, *ApJ*, 696, L98
- Rosenthal, L. J., Knutson, H. A., Chachan, Y., et al. 2022, *ApJS*, 262, 1
- Skrutskie, M. F., Jones, T., Hinz, P., et al. 2010, in *Ground-based and Airborne Instrumentation for Astronomy III*, ed. I. S. McLean, S. K. Ramsay, & H. Takami, Vol. 7735, International Society for Optics and Photonics (SPIE), 77353H
- Soubiran, C., Jasniewicz, G., Chemin, L., et al. 2018, *A&A*, 616, A7
- Soummer, R., Pueyo, L., & Larkin, J. 2012, *ApJ*, 755, L28
- Storn, R. & Price, K. 1997, *Journal of Global Optimization*, 11, 341
- Takeda, G. & Rasio, F. A. 2005, *ApJ*, 627, 1001
- Torres, G. 1999, *PASP*, 111, 169
- van Leeuwen, F. 2007, *A&A*, 474, 653
- Vigan, A., Fontanive, C., Meyer, M., et al. 2021, *A&A*, 651, A72
- Voges, W., Aschenbach, B., Boller, T., et al. 1999, *A&A*, 349, 389
- Voges, W., Aschenbach, B., Boller, T., et al. 2000, *IAU Circ.*, 7432, 3
- Weidenschilling, S. J. & Marzari, F. 1996, *Nature*, 384, 619
- Wu, Y. & Murray, N. 2003, *ApJ*, 589, 605
- Zacharias, N., Finch, C. T., Girard, T. M., et al. 2012, *VizieR Online Data Catalog*, I/322A